An Integrated, Software-Defined FDD Transceiver: Distributed Duplexing Theory and Operation

Thomas Tapen, *Student Member, IEEE*, Hazal Yüksel, *Student Member, IEEE*, Zachariah Boynton, *Student Member, IEEE*, Alyssa Apsel, *Senior Member, IEEE*, and Alyosha Molnar, *Senior Member, IEEE*

***Abstract*— Implementing flexible, software-defined duplexing transceivers remains challenging due to the inherent self-interference from TX to RX that requires cancellation in the RF/analog domain. Previously, we presented a novel, duplexing, integrated, single antenna transceiver architecture that used an M-stage distributed amplifier combined with an artificial transmission line to achieve high transmit-receive isolation across more than an octave in center frequency. In this paper, we explain and explore the trade-offs and limits on this class of distributed, duplexing transceivers as a function of system and sub-circuit parameters.**

***Index Terms*— Distributed amplifier, FDD, full-duplex, passive mixer, software-defined, transmission line, transceiver, tunable, TX-RX isolation, wide-band.**

I. Introduction

As WIRELESS data demands increase, flexible wireless systems are a virtual necessity. Making use of whitespace spectrum (e.g. unused satellite and TV bands) requires the utilization of transceivers that can support a multitude of bands. Furthermore, existing spectrum can be used more efficiently with hardware that supports frequency division duplexing (FDD) as is required for most cellular standards, including W-CDMA (3G) and 4G LTE. These solutions have inherent challenges, and current state of the art multi-band, software-defined FDD systems use multiple antennas and/or multiple off chip duplexers, which dramatically increase the system's cost and size while limiting its flexibility [1]–[10].

Integrated, narrowband duplexers that achieve both high isolation and high TX output power with a single antenna port have been previously demonstrated [11]–[15], however maintaining high isolation and output power over multiple octaves of tuning range within these constraints has proven to be difficult. These challenges are exacerbated by the need for high TX power efficiency and low receiver noise figure. [16] has demonstrated a combination of techniques that can provide suppression of both TX RF signals and TX noise at the receiver. This system uses a distributed structure to isolate TX and RX and requires only a single antenna port while being tunable across multiple octaves.

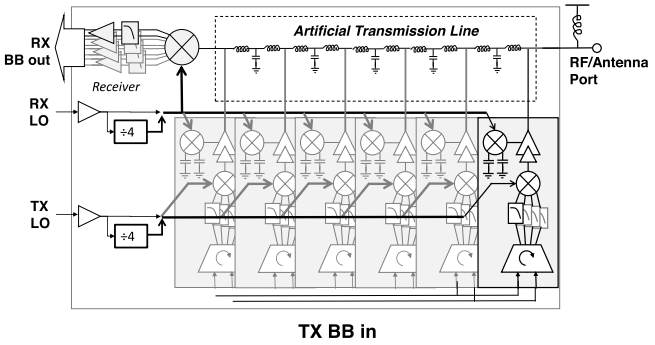

Fig. 1. Block diagram of the system from [16].

In this paper, we provide a full theoretical analysis of the distributed duplexing systems presented in [16] and [17]. We analyze: **1.** The fundamental behavior of a distributed duplexing transceiver. **2.** Methods for selecting the complex weights to null the transmitter signal at the receiver while optimizing TX efficiency. **3.** The trade-off space of weight precision, number of stages, tuning range, and various circuit parameters. **4.** The effects of TX output noise on RX NF.

II. The Distributed Transmitter

The duplexing transceiver shown in Figure 1 (from [16]) can be thought of as an extension of a distributed amplifier [18]. In a distributed amplifier such as the one in Figure 2, the outputs of M sub-transmitters are combined by a passive network—often a transmission line or similar LC structure. The inputs are phase shifted relative to each other such that the TX signal V_{in} adds constructively at the antenna port. In a traditional distributed amplifier, these input phase shifts are provided by a second transmission line, but the fundamental operation of the amplifier is the same however the appropriate phase shifts are generated. More generally, these input phase shifts can be treated as complex input weights with both a gain and phase term.

A distributed amplifier used as in Figure 2 will provide some TX/RX rejection (P_{RX}/P_{ANT}) at the RX port, but high rejection only appears at a few frequencies, and between

Manuscript received May 24, 2019; revised August 27, 2019; accepted September 10, 2019. Date of publication December 12, 2019; date of current version January 15, 2020. This material is based in part upon work supported by the DARPA Class program, Google, and NSF Grants 1247915 and 1641100. This article was recommended by Associate Editor M. Onabajo. *(Corresponding author: Thomas Tapen.)*

T. Tapen, Z. Boynton, A. Apsel, and A. Molnar are with the Department of Electrical and Computer Engineering, Cornell University, Ithaca, NY 14853 USA (e-mail: tpt26@cornell.edu).

H. Yüksel is with the Department of Electrical Engineering, Columbia University, New York, NY 10027 USA.

Color versions of one or more of the figures in this article are available online at http://ieeexplore.ieee.org.

Digital Object Identifier 10.1109/TCSI.2019.2945134

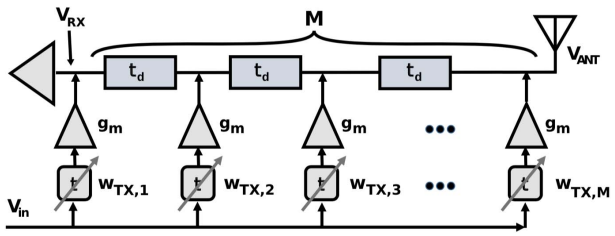

Fig. 2. A typical distributed amplifier being used as a duplexer. A distributed transmitter is simply this system with full software control of each $w_{TX,i}$.

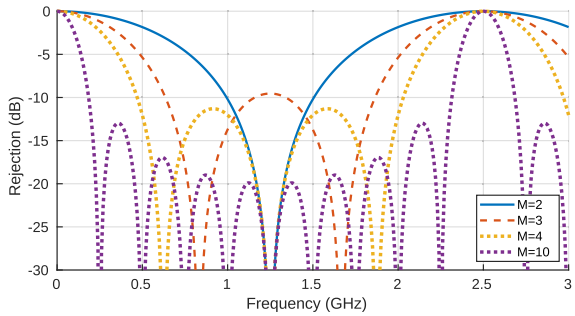

Fig. 3. The rejection achieved by a typical distributed amplifier across frequency and number of taps (M) for an ideal, lossless transmission line with $\tau_d = 200$ps per stage [19]. By our definition, rejection $= 1/(\text{isolation}) = P_{RX}/P_{ANT}$.

these frequencies degrades to around 10-15dB as shown in Figure 3. This is insufficient for FDD operation [13]. However, by manipulating the input weights $w_{TX,i}$, greater TX/RX rejection can be achieved over a wide tuning range with a minimal impact on TX output power.

A. Combiner Modeling and Weight Calculation

The passive network that combines the TX signals can be described as an impedance matrix (**Z**), derived from enforcing Kirchoff's Current Law (KCL) at each sub-transmitter output in Figure 2. **Z** has as many rows and columns as there are current-mode transmitter taps. If the voltage on individual taps are not of interest, then this can be compacted into a 2xM matrix ($\mathbf{Z_{TL}}$), with M columns for the M inputs, and two rows corresponding to the receiver and antenna node voltages.

$$\mathbf{Z_{TL}} = \begin{bmatrix} \partial v_{RX}/\partial i_1 & \partial v_{RX}/\partial i_2 & \dots & \partial v_{RX}/\partial i_M \\ \partial v_{ANT}/\partial i_1 & \partial v_{ANT}/\partial i_2 & \dots & \partial v_{ANT}/\partial i_M \end{bmatrix} \quad (1)$$

where i_n is the current flowing into the n$^{\text{th}}$ transmission line tap.

Optimizing isolation (P_{ANT}/P_{RX}) requires choosing the weights associated with individual transmitters given this impedance matrix. The first row of the impedance matrix ($\overrightarrow{Z_{RX}}$) describes how injected currents combine at the receive port, and the second row ($\overrightarrow{Z_{ANT}}$) describes how they combine at the antenna port. Treating the transconductances of sub-PAs as a diagonal MxM matrix $\mathbf{G_m}$, and the tap weights as an M-entry column vector, $\overrightarrow{w_{TX}}$:

$$\begin{bmatrix} V_{RX} \\ V_{ANT} \end{bmatrix} = \mathbf{Z_{TL}}\mathbf{G_m}\overrightarrow{w_{TX}}V_{in} = \begin{bmatrix} \overrightarrow{Z_{RX}} \\ \overrightarrow{Z_{ANT}} \end{bmatrix}\mathbf{G_m}\overrightarrow{w_{TX}}V_{in} \quad (2)$$

Choosing a weight vector $\overrightarrow{w_{TX}}$ properly achieves suppression at the RX port and summation at the TX port. A simple mathematical solution is to set $V_{ANT} = 1$ and $V_{RX} = 0$ and to solve for $\overrightarrow{w_{TX}}$ using the Moore-Penrose pseudo-inverse of $\mathbf{Z_{TL}}$:

$$\overrightarrow{w_{TX}} = (\mathbf{Z_{TL}}\mathbf{G_m})^*[\mathbf{Z_{TL}}\mathbf{G_m}(\mathbf{Z_{TL}}\mathbf{G_m})^*]^{-1}\begin{bmatrix} V_{RX} \\ V_{ANT} \end{bmatrix} \quad (3)$$

Equation 3 by itself provides little intuition. However, it is easy to see that we want to choose $\overrightarrow{w_{TX}}$ such that it is orthogonal to $\overrightarrow{Z_{RX}}$, so that their product (the voltage at the RX port) is zero. At the same time, $\overrightarrow{w_{TX}}$ should be reasonably well aligned with the classic distributed amplifier weights ($\overrightarrow{Z^*_{ANT}}$) to ensure TX signal combines mostly in-phase at the antenna port. A reasonable choice of $\overrightarrow{w_{TX}}$ is to make it parallel to $\overrightarrow{Z^*_{ANT}}$, and then subtract the projection of this vector onto $\overrightarrow{Z^*_{RX}}$, such that:

$$\overrightarrow{w_{TX}} \propto \overrightarrow{Z^*_{ANT}} - \overrightarrow{Z^*_{RX}}\left(\frac{\overrightarrow{Z_{RX}}\cdot\overrightarrow{Z^*_{ANT}}}{\overrightarrow{Z_{RX}}\cdot\overrightarrow{Z^*_{RX}}}\right) \quad (4)$$

scaled by the overall desired gain.

This is simply the Gram-Schmidt process for finding a set of orthonormal basis vectors and is equivalent to using a pseudo-inverse (equation 3). All of these equivalent methods find the solution to $\overrightarrow{w_{TX}}$ that achieves the desired V_{ANT} while minimizing $||\overrightarrow{w_{TX}}||_2$. True optimization for system power efficiency is not necessarily achieved by minimizing $||\overrightarrow{w_{TX}}||_2$, but this minimization provides a reasonable solution. System power efficiency is considered in more detail in Section II-E.

B. Distributed Amplifier Isolation Across Frequency

For a transmission line combiner, two important choices are the number of current-injection taps, and the propagation delay between each tap. Some insight into these decisions can be found by looking at a classic distributed amplifier. Assuming an ideal, lossless transmission line whose segments have a time delay τ_d, and characteristic impedance Z_0 (and assuming matching at the RX and antenna port), we can find $\mathbf{Z_{TL}}$:

$$\mathbf{Z_{TL}} = \left(\frac{Z_0}{2}\right)\begin{bmatrix} 1 & e^{(-j\omega\tau_d)} & \dots & e^{(-j(M-1)\omega\tau_d)} \\ e^{(-j(M-1)\omega\tau_d)} & \dots & e^{(-j\omega\tau_d)} & 1 \end{bmatrix} \quad (5)$$

and choose $\overrightarrow{w_{TX}}$ so that V_{ANT} is maximized:

$$\overrightarrow{w_{TX}} = \begin{bmatrix} e^{(j(M-1)\omega\tau_d)} \\ \vdots \\ e^{(j\omega\tau_d)} \\ 1 \end{bmatrix} \quad (6)$$

The resulting rejection at the RX port is plotted in Figure 3. In this case, we see that the lowest frequency where perfect isolation occurs is $\omega_{min} = \pi/(M\tau_d)$. Similarly perfect isolation occurs at integer multiples of ω_{min} up to $\omega = \frac{\pi}{\tau_d}$, at which point each transmission line segment gives a 180° phase shift and isolation degrades entirely. More generally, if $\omega\tau_d$ corresponds to a phase shift of $k\pi$ where $k \in \mathbb{Z}$, isolation will degrade to 0dB, as can be seen in Figure 3 at DC ($k = 0$) and 2.5GHz ($k = 1$). Empirically, it can also be observed that isolation degrades between optimal frequencies

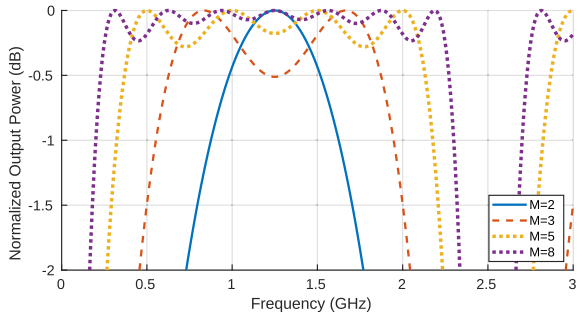

Fig. 4. Normalized P_{ANT} across frequency if the TX weights are set by equation 3 and scaled for a constant L-2 norm. Plotted for an ideal, lossless transmission line and $\tau_d = 200$ps.

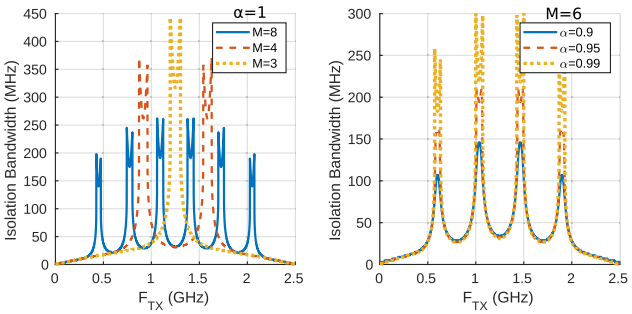

Fig. 5. Bandwidth over which isolation ≥40dB for $\tau_d = 200$ps and varying M and α. Depending on f_{TX}, rejection bandwidth ranges from 20MHz to 300MHz.

(to ∼10dB for $M = 3$). The band between the highest and lowest frequency of perfect isolation for $M \geq 2$ is $f_{max}/f_{min} = M - 1$. If the minimum level of ∼10dB of isolation is allowed, the frequency range extends roughly to $f_{max}/f_{min} \approx M$ for $M \geq 3$.

C. Frequency Range and Combining Efficiency

The basic analysis above indicates how much "natural" isolation one can expect from the distributed structure on its own. One can achieve perfect isolation by adjusting the transmit weights, provided $\omega\tau_d$ is not a multiple of 180°. However, changing the transmit weights away from the ideal values for coherent summation at the antenna port will be inherently less efficient. We define the efficiency with which each sub-transmitter's output currents are combined at the antenna port as the "combining efficiency" η_{comb}:

$$\eta_{comb} = \frac{I_{ANT}}{I_{ANT,ideal}} = \frac{I_{ANT}}{\sum_{i=1}^{M} I_{TX,i}} \tag{7}$$

where $I_{TX,i}$ is the ith sub-transmitter's output current signal, and I_{ANT} is the total output current at the antenna port.

To analyze this limited combining efficiency, we can calculate TX weights for perfect rejection using equations 3 and 5 at each frequency. We know that these weights give zero TX power at the RX input, but plotting the resulting TX output power at the antenna port (P_{ANT}) shows variation across frequency (Figure 4). For each frequency where the distributed amplifier provides perfect rejection (Figure 3), $\eta_{comb} = 1$ and output power reaches a maximum. At all other frequencies, some of the otherwise available TX output power is sacrificed to ensure perfect TX rejection at the RX port. If we define a function $\text{Rej}_{\text{int}}(\omega)$ that gives the intrinsic rejection expected from a distributed amplifier (Figure 3), and the maximum possible output power assuming perfect TX summation (P_{max}) we can calculate the expected drop in TX output power:

$$P_{ANT} = P_{max}\left(1 - \text{Rej}_{\text{int}}(\omega)\right) \tag{8}$$

Therefore, the combining efficiency of distributed duplexing is related to the intrinsic rejection, and is maintained over a similar bandwidth. Furthermore, combining efficiency is improved within this band as the number of stages increases. $\eta_{comb} > 90\%$ can be achieved over more than an octave for any case where $M \geq 3$. Low combining efficiency will lower the overall system power efficiency, but is only one factor affecting the overall efficiency (see Section II-E).

D. Isolation Bandwidth for Fixed TX Weights

In the previous two sections, we have discussed how the combining network sets the bandwidth over which a distributed duplexer is tunable. For each desired transmit frequency (f_{TX}) within this bandwidth, there exist choices for $\overrightarrow{w_{TX}}$ that provide high isolation without a large cost to output power. However, given a fixed choice of $\overrightarrow{w_{TX}}$, high TX/RX isolation is achieved in a narrower bandwidth around f_{TX}. This limited bandwidth occurs because the phase shift imparted by each transmission line segment varies as frequency varies, so isolation degrades as frequency varies around f_{TX}.

We define isolation bandwidth (or equivalently, rejection bandwidth) as how TX-RX isolation deteriorates around f_{TX} given a fixed $\overrightarrow{w_{TX}}$, M, and τ_d. Figure 5a shows this for varying M. We also introduce a term α, which models the loss from each transmission line segment. Including α, the expression for $\mathbf{Z_{TL}}$ becomes:

$$\mathbf{Z_{TL}} = \left(\frac{Z_0}{2}\right) \times \begin{bmatrix} 1 & \alpha e^{-j\phi} & \dots & \alpha^{M-1}e^{-j(M-1)\phi} \\ \alpha^{M-1}e^{-j(M-1)\phi} & \dots & \alpha e^{-j\phi} & 1 \end{bmatrix} \tag{9}$$

Using this definition of $\mathbf{Z_{TL}}$, Appendix shows how the rejection around f_{TX} can be derived using the pseudo-inverse method, and the result is shown in equation 10.

To see how much isolation bandwidth can be expected across different values of f_{TX}, we choose a threshold for sufficient isolation of 40dB. In Figure 5 we plot the bandwidth around f_{TX} for which the isolation will be higher than the 40dB threshold for different values of M and α. In general, there are two typical situations for isolation bandwidth. Representative plots of these two cases are plotted in Figure 6. In general, a single rejection notch exists and high isolation is achieved over a small bandwidth (for a threshold of 40dB isolation, only about $1/(200\tau_d)$). However, for some choices of f_{TX}, two rejection notches happen to appear near each other, and the isolation bandwidth is increased greatly over the nominal case for the same isolation threshold. For M stages, Figure 5 shows there are M-2 regions between "natural"

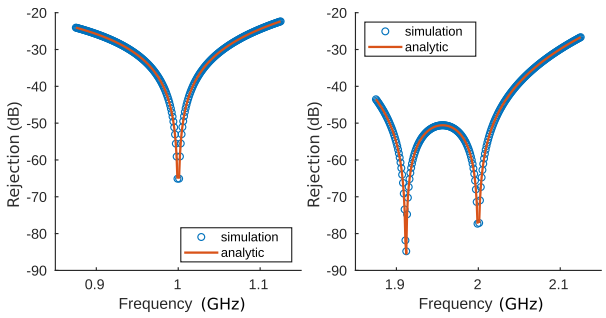

Fig. 6. Two representative cases for rejection bandwidth are shown. One rejection notch is guaranteed at f_{TX}. In some cases, a secondary rejection notch exists near the one at f_{TX} (as shown in the right plot where $f_{TX} = 2$GHz), increasing the bandwidth for which good rejection is achieved. Both plots are shown for $\alpha = 1$, M = 7, and $\tau_d = 200$ps, and show both simulation data and the analytic expression in equation 10.

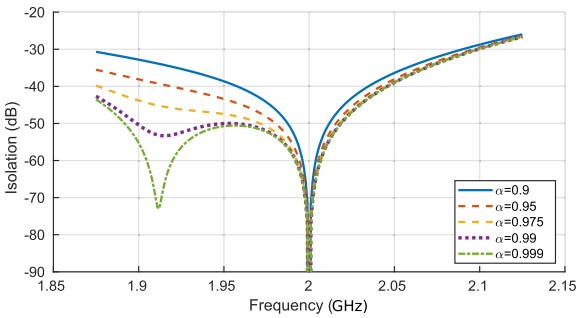

Fig. 7. Rejection at 2GHz for M = 7 and $\tau_d = 200$ps including loss in the transmission line. Even for low loss, the secondary rejection notch begins to disappear, eventually limiting rejection bandwidth in the 2-notch scenario.

isolation peaks where high isolation bandwidth is achievable, though as M increases, the bandwidth within these regions decreases. Additionally, as the transmission line loss increases, any secondary notches disappear, causing the high-isolation bands to shrink (Figures 5 and 7).

Regardless of the properties of the high-isolation bandwidth regions, there is a minimum isolation bandwidth guaranteed across frequency. This bound is given in equation 11, and can be derived from equation 10 by setting $M = 2$, $\alpha = 1$, and assuming $\Delta\phi$ is small:

$$\text{IsoBW}(f_{TX}) \geq \frac{2 \cdot 10^{(\text{Rej}_{min}/20)} \sin(2\pi f_{TX} \tau_d)}{\pi \tau_d} \tag{11}$$

where Rej_{min} is the minimum acceptable rejection in dB.

E. Optimizing Efficiency of Weights

In the simple projection approach to finding optimal transmitter weights from Section II-A, the resulting weights are not only orthogonal to $\overrightarrow{Z_{RX}}$, guaranteeing that TX signal will be nulled at the RX port, but also provides the desired TX signal while minimizing L-2 norm of the weights. This minimization is a reasonable proxy for maximizing efficiency, as the sub-transmitter PAs will dominate power consumption, and will consume power proportional to the TX weights. However, optimizing system efficiency is better done by considering the L-1 norm of the weights, since the total PA bias current is proportional to $||\overrightarrow{w_{TX}}||_1$. To perform proper optimization of system power efficiency (P_{ANT}/P_{DC}), we must first find P_{DC}.

One bound on power consumption (P_{DC}) is set by both the current signal in each PA, and the voltage signal on its output. Thus the expected power consumption will be the sum of the product of each PAs current and voltage, summed across PAs:

$$P_{DC} \propto \sum_{k=1}^{M} |v_k||i_k| \tag{12}$$

In this case, if bias current and voltage for each PA is made equal to peak signal current and voltage, each PA will be operated in the ideal Class A mode, so the expected maximum efficiency is 50%. Note that these PAs can be operated in a less linear, more efficient mode, but overall trends we will observe would still hold. Optimizing TX weight selection to minimize $||\overrightarrow{w_{TX}}||_1$ was done using a stochastic approximation algorithm with a local gradient descent. Simulation in MATLAB using this optimization algorithm (Figure 8) shows that using this definition of efficiency indeed provides a moderate improvement over the projection method above, with qualitatively similar behavior across frequency and number of amplifier stages. Interestingly, the optimal weight vector tends to be sparse (i.e. some weights are zero). In contrast, simple projection is entirely non-sparse (every weight has significant magnitude) except where $\eta_{comb} \approx 1$. This sparsity has important implications for system efficiency since zero-weights imply that entire sub-transmitters could be shut down without degrading performance, thus saving significant overall power outside the PAs. For the scenario in Figure 8, the median number of active PAs when $\eta_{comb} \geq 90\%$ is 5, so typically one of the 6 PAs in that scenario could be off for most frequencies of operation.

III. Transmission Line Optimization

All delay elements considered thus far have assumed a pure time delay implemented with a transmission line structure. However, in reality the physical implementation of these delays will impact the system performance and may not achieve an constant time delay. As discussed in section II-B, $\tau_d \geq \pi/(M\omega_{min})$ if ω_{min} is the minimum desired transmit frequency. This corresponds to a required total phase shift ($(M-1)\omega\tau_d$) of 90° to 180°. In the low GHz design space,

$$\text{Rej}(f_{TX} + \Delta f) = 20\log_{10}\left(\alpha^{M+1}\left|\frac{K_\alpha(\alpha^{2M}-1)e^{j\phi} - \left(\frac{\sin(M\phi)}{\sin(\phi)}\right)L_\alpha(\alpha^2-1)e^{jM\phi}}{L_\alpha\alpha^2(\alpha^{2M}-1)e^{jM\phi} - \left(\frac{\sin(M\phi)}{\sin(\phi)}\right)\alpha^{2M}(\alpha^2-1)K_\alpha e^{j\phi}}\right|\right), \quad \phi = 2\pi f_{TX}\tau_d,$$
$$K_\alpha = \left(e^{j\Delta\phi} - \alpha^2\right)\left(e^{jM(2\phi+\Delta\phi)} - 1\right), \qquad L_\alpha = \left(e^{jM\Delta\phi} - \alpha^{2M}\right)\left(e^{j(2\phi+\Delta\phi)} - 1\right), \quad \Delta\phi = 2\pi(\Delta f)\tau_d \tag{10}$$

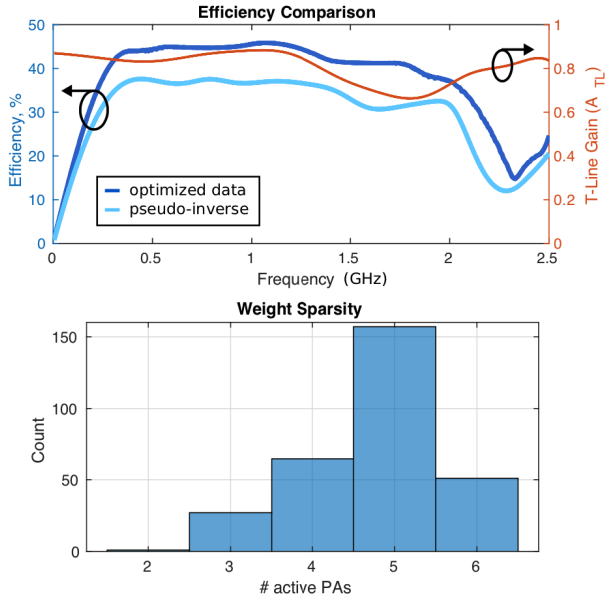

Fig. 8. Comparison of power efficiency for the typical pseudo-inverse weight calculation and for optimized PA bias based on equation 12. The system is unable to achieve the ideal 50% efficiency due to transmission line loss and $\eta_{comb} < 1$. This plot is given for M = 6, n = 3, L = 3.333nH, Q = 20, $R_{sh} = 1\text{k}\Omega$ and uses the lossy LC transmission line model from Section III-C. A histogram of the weight sparsity for the optimized case is also plotted, showing at least one PA is off in most cases after efficiency optimization for the frequencies where $\eta_{comb} \geq 90\%$.

a transmission line capable of providing $\geq 90°$ of delay would need to be several millimeters long and would be impractical for integrated systems. In order to achieve the delay required in an integrated form-factor an artificial transmission line can be used. The rest of this section will be dedicated to the analysis of such an artificial line on system performance.

A. Frequency Range

In addition to the previously discussed frequency limits imposed by combining efficiency, an artificial transmission line has a cutoff frequency (i.e. the Bragg frequency). Above this frequency, the artificial transmission line cuts off like a low-pass filter. The filter's stopband begins around $f_{Bragg} \approx 1/(\pi\sqrt{LC})$, so high insertion loss and poor S_{11} can be expected near and above this frequency, making it important to design an artificial transmission line with its Bragg frequency well above the upper combining efficiency limit.

If the Bragg frequency is too low for a given M and τ_d, it can be increased by using n artifical transmission line segments per sub-transmitter, each with delay $\tau_{unit} = \tau_d/n$ (Figure 9). Assuming this structure we find the Bragg frequency as a function of n and τ_d:

$$f_{max,TL} \equiv \xi f_{Bragg} \approx \frac{\xi}{\pi\sqrt{LC}} \approx \frac{\xi}{\pi\,\tau_{unit}} = \frac{n\xi}{\pi\,\tau_d} \tag{13}$$

where $\xi \in [0, 1]$ is chosen by the designer to decide how close to the Bragg limit is acceptable.

To decide the value n should take given M and τ_d, we must look at the maximum frequency limit due to the drop in combining efficiency as $\phi \rightarrow 180°$. This limit ($f_{max,\eta}$) can be considered to be roughly the highest frequency at

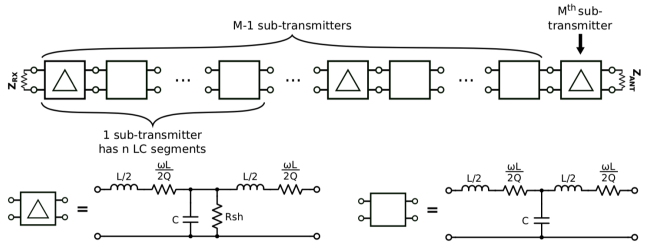

Fig. 9. Configuration of the artificial transmission line for general n and M. Each LC segment is represented by a passive 2-port network. Where sub-transmitter PAs connect to the transmission line, the PAs output resistance (R_{sh}) is modeled.

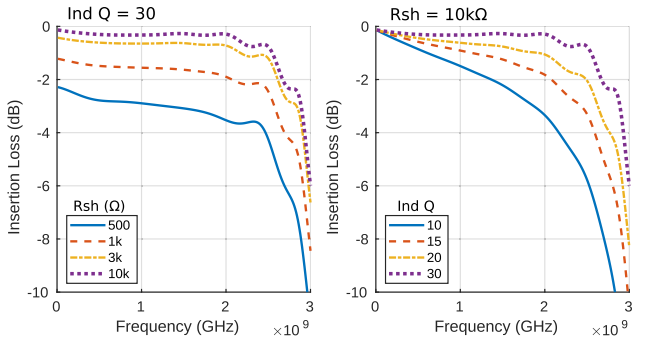

Fig. 10. Simulated insertion loss across frequency for $Z_0 = Z_{RX} = Z_{ANT} = 50\Omega$, $\tau_d = 200$ps, $n = 2$, and $M = 4$ across PA output resistance (R_{sh}) and inductor Q. Low R_{sh} and low inductor Q increase insertion loss below $f_{Bragg} \approx 3.2$GHz.

which perfect isolation is achievable in a standard distributed amplifier. From Section II-B that means:

$$f_{max,\eta} \equiv \frac{1}{2\tau_d} - \frac{1}{2\tau_d M} = \frac{M-1}{2\tau_d M} \tag{14}$$

for $M \geq 2$. To find n, we set $f_{max,TL} = f_{max,\eta}$:

$$n = \frac{\pi(M-1)}{2\xi M} \tag{15}$$

Here we can see that if $n = 1$, the Bragg limit will limit the maximum frequency for $M \geq 3$ even if $\xi = 1$, and so typically $n \geq 2$ should be used.

B. Insertion Loss

Ideally, the transmission line structure would be lossless. In practice, the dominant sources of loss are the resistive losses associated with the inductors and the finite output resistance of the sub-transmitter PAs. The expected insertion loss can be found by treating each transmission line segment as a 2-port network and finding the S_{21} of N cascaded segments. As shown in Figure 9, we find $N = n(M-1)+1$. One complicating factor is that if $n \neq 1$, some transmission line segments will include shunting loss due to PA output resistance, while others will not (Figure 9). Figure 10 shows the effect of inductor Q and PA output impedance (R_{sh}) for a specific choice of n, M, and τ_d.

It is worth noting that when lengthening the line with constant n and M, loss will increase, however this is typically not how more stages would be added to a design. As discussed in Section II-B, the total required line delay is set by the lowest desired frequency of operation. If the line is of constant length

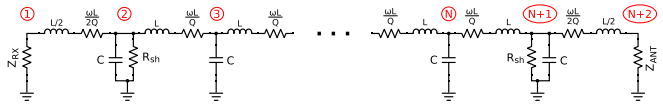

Fig. 11. Equivalent circuit of an artificial transmission line for $n = 2$ with node numbers labeled.

and we consider loss from the series inductors, splitting the line into more and more segments (increasing n and/or M), doesn't change the total series inductance. Therefore, given a constant inductor Q, the line loss due to the inductors doesn't depend on n and M, but rather the minimum frequency of operation set by the total delay $M\tau_d$.

Of course, as more sub-transmitters are added, more copies of the PA output impedance R_{sh} appear in parallel, which would also seem to increase loss as M increases. This is true, however if a constant maximum output power is desired, increasing M requires more sub-transmitters with lower individual output power requirements. For lower power sub-transmitters, R_{sh} can be improved proportionally and insertion loss is once again roughly constant over changing M, assuming a constant maximum output power at the antenna (P_{ANT}). The requirements imposed on the sub-transmitters by distributed duplexing and the relationship between output current and R_{sh} are explained in Section IV.

Considering a system with a specific requirement for P_{ANT} and for the minimum frequency of operation, we can say that insertion loss is independent of n and M to first order. This suggests that large n and M are desirable, however Section IV will discuss how sub-transmitter constraints limit the maximum practical n and M.

C. Modeling the Artificial Transmission Line

The expression for $\mathbf{Z_{TL}}$ in equation 9 will be approximately accurate for an artificial transmission line, however it only models the line well if the frequency of interest is well below $f_{max,TL}$, and only if a narrow bandwidth is considered due to the fact that τ_d and α vary with frequency for an artificial transmission line. Considering that one of the strengths of a distributed transmitter is the wide bandwidth over which it is tunable, a model that is only accurate for a narrow bandwidth is not ideal. Therefore, we can derive a more accurate $\mathbf{Z_{TL}}$ for artificial transmission lines using the circuit in Figure 9.

To efficiently derive $\mathbf{Z_{TL}}$, we start by noticing that many of the circuit nodes in Figure 9 are simply points where two of the series L/2 inductors meet. If these two series L/2 inductors are combined into a single inductor of value L, we arrive at an equivalent circuit of the form shown in Figure 11. If N corresponds to the number of T-networks used as before, the resulting circuit has N+2 nodes, where the extra 2 nodes are the RX and antenna ports.

To fully model the circuit in Figure 11, we first consider an impedance matrix $\mathbf{Z}$ of dimension N+2 by N+2 derived from enforcing KCL at each node. Deriving $\mathbf{Z}$ directly is potentially very tedious, so we will instead find the admittance matrix $\mathbf{Y}$, where $\mathbf{Y} = \mathbf{Z}^{-1}$. To find the entries of $\mathbf{Y}$, we use the definition of the admittance parameter (y-parameter) for a general N-port network:

$$y_{i,j} = \frac{I_i}{V_j}\Big|_{V_{k\neq i}=0} \tag{16}$$

Performing this analysis on each node and noting that only adjacent nodes have non-zero admittance parameters, we can see that the Y-matrix is a square, banded matrix of the form:

$$\mathbf{Y} = \begin{bmatrix} y_{11} & y_{12} & & & 0 \\ y_{21} & y_{22} & y_{23} & & \\ & y_{32} & y_{33} & \ddots & \\ & & \ddots & \ddots & y_{N+1,N+2} \\ 0 & & & y_{N+2,N+1} & y_{N+2,N+2} \end{bmatrix} \tag{17}$$

where each entry is given by the following formulae after applying the definition of $y_{i,j}$:

$$\begin{aligned} y_{i,i} &= \begin{cases} 2Y_s + j\omega C + \dfrac{1}{R_{sh}} & \text{nodes with PAs} \\ 2Y_s + j\omega C & \text{nodes without PAs} \end{cases} \\ y_{i\pm1,i} &= y_{i,i\pm1} = -Y_s \quad i \in [3, N] \\ Y_s &\equiv \frac{1}{\omega L(j + 1/Q)} \end{aligned} \tag{18}$$

For $i = 1, 2, N+1, N+2$, the pattern in equation 18 doesn't hold. Applying the y-parameter definition once more for these remaining nodes gives:

$$\begin{aligned} y_{N+2,N+2} &= 2Y_s + \frac{1}{Z_{ANT}} \qquad y_{1,1} = 2Y_s + \frac{1}{Z_{RX}} \\ y_{N+1,N+1} &= y_{2,2} = j\omega C + 3Y_s + \frac{1}{R_{sh}} \\ y_{N+1,N+2} &= y_{N+2,N+1} = y_{1,2} = y_{2,1} = -2Y_s \end{aligned} \tag{19}$$

At this point, every non-zero value of $\mathbf{Y}$ has been defined, so we can find $\mathbf{Z}$ by inverting $\mathbf{Y}$.

This gives us the N+2 by N+2 impedance matrix ($\mathbf{Z}$) that fully describes the circuit in Figure 11. $\mathbf{Z_{TL}}$ can be found simply by taking the relevant terms from $\mathbf{Z}$—specifically keep only the first and last rows of $\mathbf{Z}$, and only keep columns with PAs connected. For the circuit in Figure 11, this means:

$$\mathbf{Z_{TL}} = \begin{bmatrix} Z_{1,2} & Z_{1,4} & \cdots & Z_{1,N+1} \\ Z_{N+2,2} & Z_{N+2,4} & \cdots & Z_{N+2,N+1} \end{bmatrix} \tag{20}$$

Using this $\mathbf{Z_{TL}}$ in place of the ideal transmission line definition of $\mathbf{Z_{TL}}$ from equation 9 is more computationally intensive, but will be accurate across frequency. One example of this is given in Figure 12, where isolation bandwidth is plotted across a wide bandwidth using both models. This plot shows how isolation bandwidth suffers due to the increasing loss at higher frequencies for an artificial line.

IV. Sub-Transmitter Constraints

As careful design of the transmission line is required to maintain the desired system-level performance, so too is the design of each sub-transmitter important. Here we will look at how system-level decisions constrain sub-transmitter design in distributed duplexers.

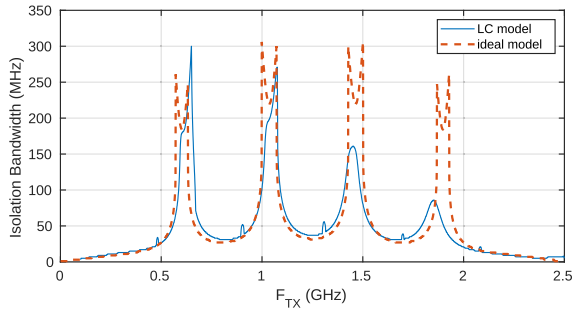

Fig. 12. Isolation bandwidth plotted using the ideal transmission line model and the LC model for an artificial line given in Section III-C. At higher frequencies, the fixed α of 0.999 chosen for the ideal model no longer models the line well. One can also see that the effective τ_d is not constant across frequency, causing the high-isolation lobes to move as frequency increases. Plotted for M = 6, n = 2, τ_d = 200ps, Q = 10, and R_{sh} = 1kΩ.

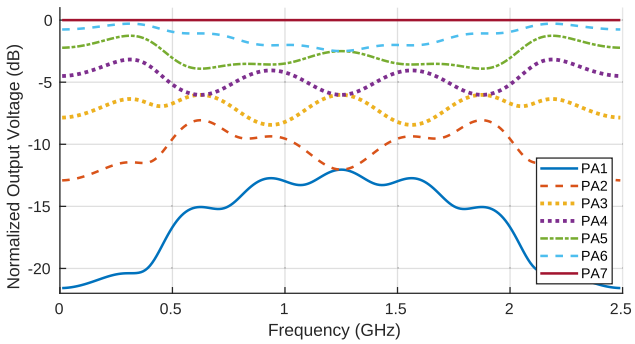

Fig. 13. Output voltage swing for each sub-transmitter for M = 8, τ_d = 200ps, and an ideal transmission line. Voltage swing decreases monotonically for all frequencies, but individual PA requirements vary across frequency. PA0 is on the RX port and is not plotted as $V_{RX} = 0$.

A. PA Restrictions

Due to both the wideband nature of distributed duplexing and the connection of each PA directly to a transmission line, certain restrictions are placed on the design of each PA. The design presented in [16] used a cascoded, Class AB, common-source amplifier, but any topology that satisfies the following requirements will work.

1) The PA must be wideband or widely tunable to span the full frequency range set by M and τ_d—potentially several octaves.

2) In order to achieve the desired maximum output power (P_{ANT}), each PA must support some maximum output current (I_{max}):

$$I_{max} > \frac{2}{\eta_{comb} M}\sqrt{\frac{2P_{ANT}}{Z_{ANT}}} \tag{21}$$

where η_{comb} is the expected combining efficiency and we assume $Z_0 = Z_{ANT} = Z_{RX}$. I_{max} must be larger than the value given in equation 21 because each PA's output will be attenuated somewhat by the transmission line's loss. If for simplicity we assume the fraction of insertion loss affecting each PA is proportional to the fractional line length seen by that PA, we can add a correction factor based on the transmission line's total power gain A_{TL}:

$$I_{max} \approx \frac{2}{\eta_{comb}}\left(\frac{A_{TL}^{\frac{1}{M-1}} - 1}{A_{TL}^{\frac{M}{M-1}} - 1}\right)\sqrt{\frac{2P_{ANT}}{Z_{ANT}}} \tag{22}$$

where equation 22 is equivalent to equation 21 in the limit as $A_{TL} \to 1$.

3) The output capacitance of the PA (C_{out}) must not interfere with the operation of the transmission line. This means C_{out} must be small enough to be absorbed into the transmission line. To maintain some transmission line impedance Z_0, the requirement for C_{out} is:

$$C_{out} \leq \frac{L}{Z_0^2} \approx \frac{\tau_{unit}}{Z_0} = \frac{\tau_d}{nZ_0} \tag{23}$$

C_{out} does not depend on M to first order because the width of PA devices can be scaled down proportionally to maintain a constant P_{ANT} as M increases. Previous sections have shown n should be large, however this constraint on C_{out} gives the upper limit on n: $n \leq \tau_d/(C_{min}Z_0)$, where C_{min} is the minimum achievable C_{out} for a given I_{max}.

4) The output resistance (R_{sh}) of the PA must be large to avoid high insertion loss in the transmission line. The effect of finite PA output resistance is modeled in Section III, where it was asserted that R_{sh} increases as M increases for a constant P_{ANT}. This is equivalent to saying that $R_{sh} \propto 1/(I_{max})$, which is true to first order because the small-signal output resistance of a FET is inversely proportional to its drain current. Therefore, insertion loss to first order does not depend on M for a fixed P_{ANT}, and so large M is desirable. Large enough M becomes impractical, due either to the breakdown of the approximate proportionalities used in the preceding discussion, or other elements of the sub-transmitter that do not scale well with M, such as the resolution (and therefore complexity) of TX weight generation (Section IV-C) and the large baseband filtering capacitors.

5) PA's must support a maximum voltage swing at their outputs (V_{max}). For the PA closest to the antenna, the voltage swing required is $V_{max} = \sqrt{P_{ANT}Z_{ANT}}$. However, given a large amount of isolation, the voltage swing close to the receiver will be near zero. Therefore one cannot simply linearly interpolate between V_{max} and 0 to find each PA's maximum voltage requirements, as generally the voltage will not decrease from antenna to receiver in equal steps. However, one can expect the maximum voltage swing to monotonically decrease moving from antenna to receiver as shown in Figure 13.

B. PA Linearity Considerations

In addition to the constraints enumerated in Section IV-A, the non-linearity of each PA will contribute harmonic terms both at the RX and antenna ports. These harmonics must be limited at the antenna port to meet spectral mask requirements, and at the RX port to avoid de-sensitizing the receiver. Due to the natural low-pass characteristic of the artificial transmission line above the Bragg frequency, high-order harmonics are filtered out. However, low-order harmonics may not be attenuated, as they may fall within the range over which the transmission line was designed to operate. In this section we will consider the implications of PA non-linearity in distributed transmitters.

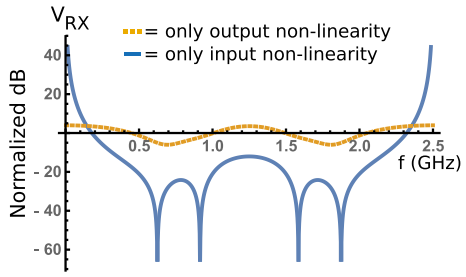

Fig. 14. The contribution of 2nd harmonic power at the RX port by PA input and output non-linearities assuming an ideal, lossless transmission line, M = 4, and τ_d = 200ps. Power is normalized so that 0dB corresponds to in-phase summation. TX weight amplitudes are scaled to maintain constant P_{ANT} at each frequency. For input nonlinearity, the TX weights provide some suppression wherever $\eta_{comb} \approx 1$ if the transmission line maintains a constant delay. Output non-linearity shows variable behavior across the usable tuning range.

Typically, output harmonic content due to PA non-linearity can be described by a polynomial function of the PA's input signal. In the case of distributed duplexing, the output harmonics of each PA must be a function of both its input and output signals, as the output swing of a specific PA may be large or small due to the action of the other sub-transmitters. Additionally, the TX weights applied to each PA's input will affect the relative phase and magnitude of harmonics as well as the fundamental tone, which will also affect the total power of harmonic terms at the RX and antenna ports.

To analyze the effects of these factors, we will first consider only non-linearity due to input signal swing and limit ourselves to 2nd order effects for simplicity. Therefore the large-signal voltage transfer function of a single PA is given by:

$$V_{out} = a_1 V_{in} + a_2 V_{in}^2 \tag{24}$$

Substituting in $V_{in} = A_{TX} \cos(\omega_{TX} t + \phi_{TX})$ to model the weighted TX signal input gives:

$$V_{out} = a_1 V_{in} + \frac{A_{TX}^2 a_2}{2} [1 + \cos(2\omega_{TX} t + 2\phi_{TX})] \tag{25}$$

Here we see that the 2nd harmonic term has a magnitude scaled by A_{TX}^2, and double the phase shift of the original signal. If we assume the transmission line provides a constant delay across frequency, then the phase shift due to transmission line propagation delay is doubled at the second harmonic as well. Because both the input signal phase shift and the phase shift from the line are doubled at the second harmonic, the resulting second harmonic signal will have the same desired phase at both the RX and antenna ports as the fundamental TX signal—implying the second harmonic (and in general, the nth harmonic) will combine in-phase at the antenna port and out-of-phase at the RX port.

Unfortunately, this does not mean that harmonics are suppressed to the same extent as the fundamental TX signal. Because the magnitude of the second harmonic term is squared, the magnitudes of each PA's contribution to V_{RX} will not be correct for cancellation unless the magnitude of each TX weight is identical. Therefore, only limited cancellation of harmonics is possible at the RX port when the TX weights have similar magnitude, as they typically do when $\eta_{comb} \approx 1$ (Figure 14).

If, instead of input non-linearity, we consider pure output nonlinearity in the same fashion, we find there is not significant suppression of non-linearity at the RX port (Figure 14). This is because the output swing monotonically increases across PAs (Figure 13), so the assumption that signal magnitudes are similar across PAs is almost always false for harmonic terms generated due to output non-linearity.

The total harmonic power at both the RX and antenna ports can be approximated by summing the input and output non-linearity terms. Because input linearity is typically a stronger effect than output linearity, there may be some modest suppression of harmonics at the RX port, but this effect depends on the relative strength of input vs output non-linearity in the specific PAs used. If the harmonic content at the RX or antenna ports is too strong, [17] presented a technique to suppress 2nd and 3rd order harmonics at the RX port in distributed duplexers implemented with 8-phase passive mixers.

C. Effects of Complex Weight Quantization

In a real sub-transmitter, the desired complex weight will be realized with limited resolution, affecting TX output power and TX/RX isolation. If we define N_b as the ENOB of control over the I and Q component of each TX weight, we can bound the peak achievable isolation as a function of N_b. To do this, we start by considering the desired nth TX signal, $V_{TX,n,ideal}$. Each $V_{TX,n,ideal}$ can be written as a sum of I and Q components like so: $V_{TX,n,ideal} = I_n + jQ_n$.

Due to quantization errors in realizing I_n and Q_n, the actual TX weight will be $V_{TX,n} = V_{TX,n,ideal} + \Delta I_n + j\Delta Q_n$. For N_b bit control on both I and Q, we can find the maximum possible value for ΔI_n and ΔQ_n:

$$\Delta I_n \leq \frac{\pm A_{max}}{2^{N_b+1}} \quad \text{and} \quad \Delta Q_n \leq \frac{\pm j A_{max}}{2^{N_b+1}} \tag{26}$$

where A_{max} is the maximum magnitude of $V_{TX,n,ideal}$.

By our definitions of $V_{TX,n}$, we can see that the magnitude of the total worst-case error for each $V_{TX,n}$ is:

$$|\Delta I_n + j\Delta Q_n| = \sqrt{\Delta I_n^2 + \Delta Q_n^2} \leq \frac{\sqrt{2} A_{max}}{2^{N_b+1}} \tag{27}$$

Given the worst-case error for a single sub-transmitter, we then find bounds on the total output signal magnitude ($|V_{ANT}|$) and TX/RX isolation. Regarding $|V_{ANT}|$, the worst-case is where all M error terms align 180° out of phase with V_{ANT}. In that case, if we define the ideal output signal as $V_{ANT,ideal}$:

$$|V_{ANT}| \geq |V_{ANT,ideal}| - M \cdot |\Delta I_n + j\Delta Q_n| \tag{28}$$

where $|V_{ANT,ideal}| = \eta_{comb} A_{max} M$. Assuming the ideal sub-transmitter weights give perfect cancellation at the RX, we can see that an error vector at the TX port will propagate down the lossless transmission line and will appear at the RX port with the same magnitude. Therefore, $|V_{RX}| \leq M \cdot |\Delta I_n + j\Delta Q_n|$ and

$$\begin{aligned} \text{Isolation} = \frac{|V_{ANT}|}{|V_{RX}|} &\geq \frac{M\,(A_{max}\eta_{comb} - |\Delta I_n + j\Delta Q_n|)}{M \cdot |\Delta I_n + j\Delta Q_n|} \\ &\geq \sqrt{2}\ \eta_{comb} \left(2^{N_b}\right) - 1 \end{aligned} \tag{29}$$

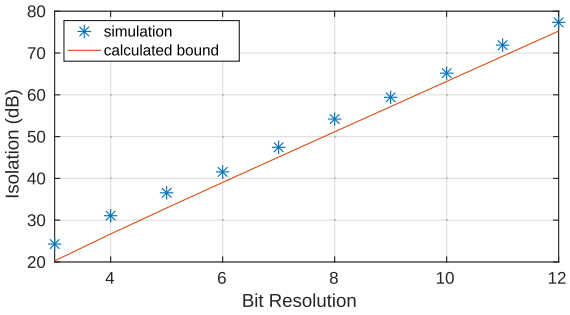

Fig. 15. Simulated worst-case isolation and the isolation bound from equation 29 versus bit resolution, where M = 6 and $\tau_d = 80$ps. The isolation bound is plotted assuming $\eta_{comb} \approx 1$. The simulation considers an ideal-lossless line from 0.8GHz to 5.5GHz—Roughly the frequency range where it is fair to assume $\eta_{comb} \approx 1$ for $\tau_d = 80$ps.

This bound is compared with a simulation of the worst-case isolation for an ideal, lossless transmission line in Figure 15. If isolation ≥40dB is desired, we can see that $N_b \geq 6$, and that 12-bit systems can theoretically achieve isolation over 70dB.

V. RX Noise Figure

Up to this point we have primarily considered the operation of a distributed duplexer with regards to preventing TX signal from interfering with the receiver. Assuming RX operation is not degraded by TX signal due to high isolation, RX NF depends on the TX output noise that reaches the receiver, as well as the transmission line's insertion loss.

A. Suppression of Correlated Noise Sources

To analyze how noise from the distributed transmitter affects the receiver, we must consider how noise from each sub-transmitter superposes at the receiver input. Depending on where in the TX chain noise is injected, there are two possibilities for how noise combines in the transmission line (Figure 16). Noise that is injected in the signal path after the TX weights have been applied is uncorrelated across sub-transmitters and does not benefit from cancelation in the combiner—it will simply RMS sum at the RX input. On the other hand, noise sources such as shared baseband drivers or oscillator phase noise that are identical across sub-transmitters will be fully correlated and will have the TX weights applied. Therefore, this correlated noise will cancel at the RX port the same way TX signal does. As discussed previously, weight selection only provides a narrowband null for TX signal, and the same is true for correlated TX noise. Therefore correlated noise will only be fully suppressed at f_{TX}. The rejection to expect for a specific TX-RX offset can be calculated the same way as isolation bandwidth (see Section II-D).

B. Low Noise Sub-Transmitter Design

The three contributors to sub-transmitter output noise are: 1) Thermal noise from the PA and BB circuits, 2) Upconverted BB flicker noise, and 3) TX LO phase noise. Close to the TX LO frequency, output noise will be dominated by upconverted BB flicker noise,and/or TX LO phase noise. In order to optimize we start by considering thermal noise and for now

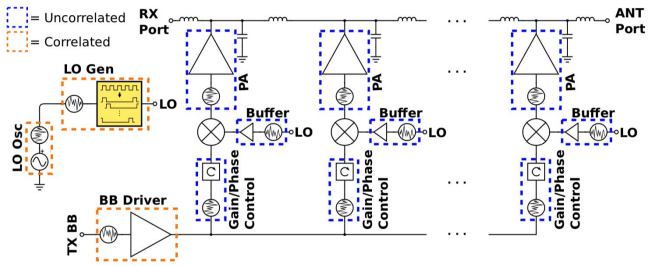

Fig. 16. Correlated and uncorrelated noise sources in a distributed transmitter. In general, any shared element's noise will be correlated across sub-transmitters, and individual sub-transmitters' noise sources will be uncorrelated.

ignore flicker and phase noise. In general, output thermal noise of a circuit will rise as gain increases. Because uncorrelated noise sources are worse than correlated ones in distributed duplexing, we should therefore concentrate gain in shared blocks as much as possible to reduce uncorrelated thermal output noise.

Using the sub-transmitter block diagram from Figure 16, this means that we would ideally have all of the TX gain in the shared baseband driver, and the gain/phase control, mixer, and PA would all have unity or lower gain. Practically speaking, we are limited by the maximum signal the baseband circuits are capable of handling without either suffering breakdown or excessive non-linearity. If we define the maximum baseband voltage amplitude as V_{swing}, we should set the output of the shared baseband driver to have amplitude V_{swing}, and have as near as possible to unity gain through the gain/phase control and mixer, thus allowing the maximum possible signal to reach the PA input. Then, given a required I_{max} (Section IV), we should use the minimum possible transconductance for the PA to minimize its thermal noise $G_{m,min} = I_{max}/V_{swing}$.

It is worth noting that if the maximum signal swing allowable is different for each sub-transmitter block, this optimization may be different. For example in [17], the upconversion mixer could not handle the full baseband driver's swing. Therefore, instead of reducing the gain of the shared baseband driver to reduce the signal amplitude, the gain/phase control block was made to have gain < 1 to reduce its uncorrelated thermal noise.

C. TX LO Phase Noise

TX LO phase noise will dominate the total TX output noise when f_{TX} is sufficiently close to f_{RX}, and will potentially degrade RX NF at any TX/RX frequency spacing. In this section, we will consider wideband uncorrelated phase noise due to sub-transmitter-specific LO circuitry, as well as more global oscillator phase noise that is strongest near f_{TX}.

For widely-spaced f_{TX} and f_{RX}, wideband, uncorrelated phase noise may dominate the total phase noise in the RX band. If this is the case, the noise at the RX input will simply be the RMS sum of each sub-transmitter's phase noise output. To avoid significantly worsening RX noise figure (NF) when TX noise is present, we can say uncorrelated phase noise must satisfy $P_{ANT} - 20\log(\eta_{comb}) + \mathrm{PN}_u(\Delta f) < P_{n,RX}$, where PN_u is the uncorrelated phase noise component

in dBc/Hz, P_{ANT} is the total output power in dBm, $\Delta f = f_{RX} - f_{TX}$ is the offset frequency, and $P_{n,RX}$ is the input-referred RX noise converted to dBm/Hz. Assuming a 50Ω system, $P_{n,RX} = 10\log(20\overline{V_{n,RX}^2})$. Because uncorrelated phase noise directly impacts RX NF, this suggests sub-transmitters should share as much LO circuitry as possible.

For closely spaced f_{TX} and f_{RX}, or when uncorrelated phase noise is kept low enough, oscillator phase noise will dominate. Assuming a single oscillator drives each sub-transmitter's LO circuitry, all oscillator phase noise will be correlated across sub-transmitter stages. Mixing correlated phase noise with weighted TX signals will generate weighted output noise, suggesting that correlated LO phase noise will be suppressed at the RX input like other correlated noise sources when $f_{TX} \sim f_{RX}$. This is correct to a certain extent, but the effects of phase noise in distributed duplexing (and indeed any similar phased arrays) is somewhat more subtle.

To analyze the effects of correlated phase noise we will consider how a phase perturbation at an offset frequency of ω_n causes output noise at the RF port of the upconversion mixer. The full phase noise spectrum is derived by sweeping ω_n and superposing the results at the output. As derived in [20, III-B], the quadrature LO including a phase perturbation at $\pm\omega_n$ is:

$$\begin{aligned} S_{LO,I} &= \cos(\omega_{LO}t) - \epsilon_n \sin[(\omega_{LO}+\omega_n)t + \phi_n] \\ &\quad - \epsilon_n \sin[(\omega_{LO}-\omega_n)t - \phi_n] \\ S_{LO,Q} &= \sin(\omega_{LO}t) + \epsilon_n \cos[(\omega_{LO}+\omega_n)t + \phi_n] \\ &\quad + \epsilon_n \cos[(\omega_{LO}-\omega_n)t - \phi_n] \end{aligned} \tag{30}$$

where ϕ_n is the random phase for this perturbation, and ϵ_n is a function of ω_n and describes the power of the perturbation at the offset ω_n. For typical oscillator phase noise, ϵ_n decreases at −20dBc/decade as ω_n increases except at very large offsets where ϵ_n is approximately constant. If we assume our quadrature input baseband voltage is given by:

$$\begin{aligned} V_{BB,I} &= A\sin[(\omega_{TX}-\omega_{LO})t + \theta] \\ V_{BB,Q} &= A\cos[(\omega_{TX}-\omega_{LO})t + \theta] \end{aligned} \tag{31}$$

then we can find the output voltage simply as:

$$\begin{aligned} V_{RF} &= V_{BB,I}S_{LO,I} + V_{BB,Q}S_{LO,Q} \\ &= A\sin(\omega_{TX}t + \theta) + \Big(\cos[(\omega_{TX}+\omega_n)t + \phi_n + \theta] \\ &\quad + \cos[(\omega_{TX}-\omega_n)t - \phi_n + \theta]\Big)A\epsilon_n \end{aligned} \tag{32}$$

Equation 32 shows that, when $\omega_n \approx \pm(\omega_{TX} - \omega_{RX})$, there will be output noise due to TX LO phase noise that appears in the RX band. However, it also shows that these noise terms pick up both the magnitude of the TX signal (A) and the phase of the TX signal (θ). This means that these noise will be suppressed around f_{TX} at the RX input due to the TX weights as expected for correlated TX noise. Because correlated noise is suppressed most strongly around f_{TX}, phase noise at small offsets (ω_n small) will be suppressed the most strongly, which also corresponds to where LO phase noise is strongest. The resulting noise spectrum at the RX input due to oscillator phase noise at small offsets therefore depends both on the shape of the LO phase noise and the TX/RX rejection. One example of what this can look like is shown in Figure 17. As with uncorrelated phase noise, we can write a requirement for small offsets to prevent TX LO phase noise from affecting RX NF. For correlated noise at an offset of $\Delta f = \pm(f_{TX} - f_{RX})$, the requirement is: $P_{ANT} - 20\log(\eta_{comb}) + \mathrm{PN}_c(\Delta f) - \mathrm{Iso}(\Delta f) < P_{n,RX}$, where $\mathrm{PN}_c(\Delta f)$ is the correlated phase noise component at offset Δf, and $\mathrm{Iso}(\Delta f)$ is the TX/RX isolation in dB at Δf.

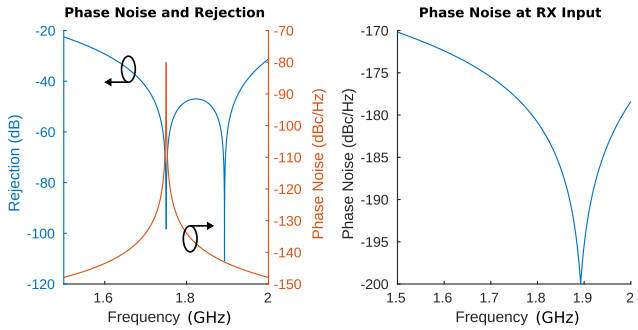

Fig. 17. The left plot shows the rejection for an ideal, lossless transmission line around $f_{TX} = 1.75$GHz, as well as purely correlated TX LO phase noise around f_{TX}. On the right, the product of these two curves is taken to find the noise spectrum at the RX input resulting from only correlated TX LO phase noise. Plotted for $M = 5$ and $\tau_d = 200$ps.

While the phase noise from smaller offsets is much stronger than that at larger offsets, the large amount of suppression for close-in phase noise means we must also consider any other offsets that may no longer be negligible. Two other values of ω_n that will produce noise in the RX band are: $\omega_n = \pm(\omega_{TX} + \omega_{RX})$. This will bring the noise terms in equation 32 to $-\omega_{RX}$. Using $\cos(\phi) = \cos(-\phi)$, this means these noise terms will be of the form $A\cos(\omega_{RX}t \pm \phi_n - \theta)$. Therefore, when $\omega_n = \pm(\omega_{TX} + \omega_{RX})$, noise will also appear in the RX band, however with the opposite phase shift ($-\theta$) of the TX signal. Reversing the phase shift of the TX weights means correlated signals/noise will tend to be suppressed at the TX port, and will add in-phase at the RX port. Therefore, while the phase noise at small offsets is suppressed by distributed duplexing, the phase noise at large offsets will be amplified (at least when $f_{TX} \sim f_{RX}$). The requirement for this "unfavorably correlated" noise is therefore approximately: $P_{ANT} + \mathrm{PN}_c(\Delta f) < P_{n,RX}$. This equation is valid for $\Delta f \approx \pm(f_{TX} + f_{RX})$ when $f_{RX} \sim f_{TX}$. Thus, extra suppression of very wideband phase noise may be needed.

To summarize, there are three categories of TX LO phase noise to consider in distributed duplexing. First is uncorrelated phase noise which must be kept very low at offsets of $\pm(f_{TX} \pm f_{RX})$ and simply RMS sums at the RX input. Second is correlated phase noise at offsets of $\pm(f_{TX} - f_{RX})$, which are suppressed by the TX signal rejection at f_{RX}. Finally, there is correlated phase noise at offsets of $\pm(f_{TX} + f_{RX})$ which add roughly in-phase unless a very wide TX-RX frequency spacing is used.

D. Calculating RX NF

To calculate the noise figure of the receiver including TX noise, we first assume a known equivalent output noise

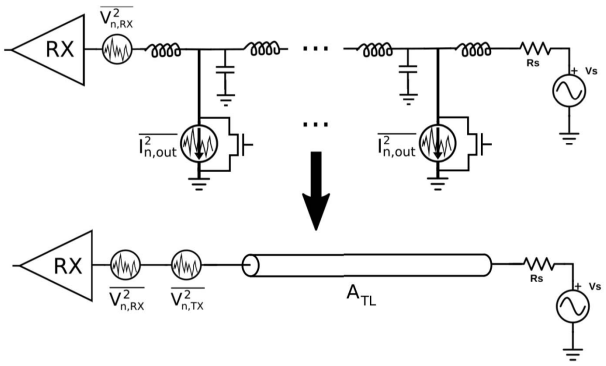

Fig. 18. The noise model for calculating RX NF. Each sub-transmmitter's equivalent output noise current superposes at the RX and are modeled as a single noise voltage: $\overline{V^2_{n,TX}}$.

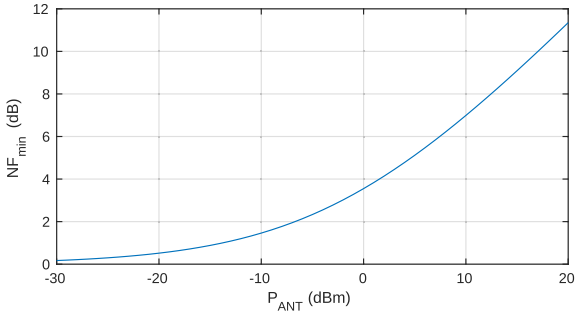

Fig. 19. The minimum RX NF due solely to PA thermal noise plotted across maximum output power. We assume PAs are designed for minimum output noise as described in section V-B given $\gamma = 1$, $Z_0 = Z_{RX} = Z_{ANT} = 50\Omega$, $V_{swing} = 0.5$V, and $A_{TL} = 1$.

current for each sub-transmitter, $\overline{I^2_{n,out}}$ (Figure 18). A noise current vector $\overrightarrow{I^2_{n,out}}$ can be used to describe the output noise from each sub-transmitter. $\overrightarrow{I^2_{n,out}}$ is composed of correlated and uncorrelated noise, so $\overrightarrow{I^2_{n,out}} = \overrightarrow{I^2_{n,c}} + \overrightarrow{I^2_{n,u}} + \overrightarrow{I^2_{n,uc}}$. We define $\overrightarrow{I^2_{n,u}}$ as the total uncorrelated output current noise, $\overrightarrow{I^2_{n,c}}$ is the total correlated output noise excluding phase noise at large offsets, and $\overrightarrow{I^2_{n,uc}}$ is the "unfavorably correlated" phase noise at large offsets. Therefore the noise injected by the TX to the RX is:

$$\overline{V^2_{n,TX}} = \overrightarrow{Z_{RX}}^{\circ 2}(\omega_{RX}) \cdot \overrightarrow{I^2_{n,out}} \approx \frac{MZ_0^2}{4}\left(\overline{I^2_{n,u}} + \mathrm{Rej}(\omega_{RX})\overline{I^2_{n,c}} + M\eta^2_{comb}\overline{I^2_{n,uc}}\right) \quad (33)$$

where $\overrightarrow{A}^{\circ b}$ denotes the b^{th} Hadamard power (i.e. termwise exponentiation) of a vector, and $\mathrm{Rej}(\omega_{RX})$ is the rejection due to TX weights also evaluated at ω_{RX}. The second expression for $\overline{V^2_{n,TX}}$ shows more intuitively how correlated noise is reduced, but is only accurate when both components of the noise power from each sub-transmitter are roughly equal (and therefore can be written as a scalar value) and transmission line loss is low. Equation 33 suggests that smaller M is better for TX noise, however this doesn't tell the full story. For a constant maximum P_{ANT} and V_{swing}, $G_{m,min}$ can be reduced as M increases. This means thermal noise (which is often a dominant noise source) and TX LO output phase noise is roughly constant for varying M at the RX input.

This total TX noise will add to the equivalent input noise of the RX ($\overline{V^2_{n,RX}}$). At the same time, loss in the transmission line will attenuate the received signal before it reaches the RX, further reducing its SNR. Using the circuit shown in Figure 18, we find the degraded RX noise factor (F):

$$F = 1 + \frac{\overline{V^2_{n,RX}} + \overline{V^2_{n,TX}}}{A_{TL}\overline{V^2_{n,s}}} \quad (34)$$

where $A_{TL} \leq 1$ and is the total power gain of the transmission line. Therefore, insertion loss in the transmission line always degrades NF, and unless $\overline{V^2_{n,RX}} >> \overline{V^2_{n,TX}}$ TX noise will also significantly degrade NF.

In general, achieving $\overline{V^2_{n,TX}} << \overline{V^2_{n,RX}}$ for high output power is not possible with this system as presented due to the uncorrelated thermal noise of each PA. If we design the PAs for minimum output noise as described in Section V-B, then we can find the minimum $\overline{V^2_{n,TX}}$ assuming only PA thermal noise:

$$\overline{V^2_{n,TX}} \approx kT\gamma\, G_m M Z_0^2 \geq \frac{2kT\gamma\, Z_0^2}{\eta_{comb} V_{swing}}\sqrt{\frac{2P_{ANT}}{Z_0}} \quad (35)$$

Plugging this minimum $\overline{V^2_{n,TX}}$ into equation 34 and setting $\overline{V^2_{n,RX}} = 0$ gives the minimum achievable RX NF in terms of output power (Figure 19). To operate with reasonable RX NF at higher P_{ANT}, [16] and [17] used an N-path PA degeneration technique to reduce each PA's transconductance in the RX band, therefore breaking the trade-off between RX NF and P_{ANT} shown in Figure 19. Any design which successfully suppresses PA thermal noise in the RX band will still have to meet the TX LO phase noise requirements, and cannot allow other noise (such as correlated baseband noise) to dominate if operation at high P_{ANT} with low RX NF is desired.

VI. Conclusion

In this paper, we have presented analysis and design considerations for the class of modified distributed amplifiers we refer to as "distributed duplexers". These considerations include the fundamental operation of distributed duplexers, the consequences using of lossy, artificial transmission lines as the combining network, optimal design of system and subcircuit parameters for best system performance, and how to characterize the added noise presented to the receiver by distributed duplexing. This paper should serve as a guide for understanding and designing distributed duplexers, and to that end we summarize the requirements for major system parameters in Table I given a desired frequency range bounded by f_{min} and f_{max} where we require $\eta_{comb} \geq 0.9$, total transmission line power gain of A_{TL}, a certain maximum output power P_{ANT}, a minimum acceptable amount of TX-RX isolation ($\mathrm{Iso}_{\mathrm{min}}$ in dB), and a matched transmission line and antenna impedance $Z_0 = Z_{ANT} = Z_{RX}$.

To verify the equations in Table I, we can design a system for $f_{min} = 900$MHz, $f_{max} = 5$GHz, and $P_{ANT} = 10$dBm.

TABLE I
DESIGN EQUATIONS FOR SYSTEM/CIRCUIT PARAMETERS

System Parameter	Design Equations
τ_d	$\frac{1}{2(M+1)f_{min}} \leq \tau_d \leq \frac{M}{2(M+1)f_{max}}$
n	$\frac{\pi(M-1)}{2\xi M} \leq n \leq \frac{\tau_d}{C_{min}Z_0}$
M	$\geq f_{max}/f_{min}$
Isolation Bandwidth	IsoBW $\geq \frac{2\cdot 10^{(-\mathrm{Iso}_{min}/20)}\sin(2\pi f_{min}\tau_d)}{\pi\tau_d}$
I_{max}	$I_{max} > \frac{2}{\eta_{comb}M}\sqrt{\frac{2P_{ANT}}{Z_{ANT}}}$
C_{out}	$C_{out} < \tau_d/(nZ_0)$
V_{max}	$V_{max} = \sqrt{P_{ANT}Z_{ANT}}$
G_m	$G_m \geq G_{m,min} = I_{max}/V_{swing}$
N_b	$N_b \geq \log_2\left[\sqrt{2}\cdot 10^{(\mathrm{Iso}_{min}/20)}/1.8+1\right]$

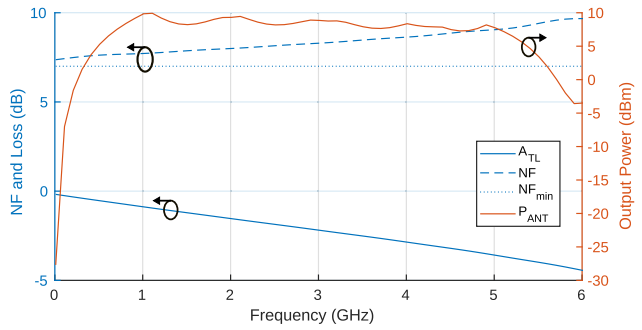

Fig. 20. P_{ANT}, NF, and A_{TL} from a MATLAB simulation of an example distributed duplexer. NF is plotted for $V^2_{n,RX} = 0$, $V_{swing} = 0.5$V, and $\gamma = 1$ as in Figure 19. The system was designed using the equations from Table I if $f_{min} = 900$MHz, $f_{max} = 5$GHz, $P_{ANT} = +10$dBm. Plotted assuming $R_{sh} = 10\text{k}\Omega$, $Z_0 = Z_{ANT} = Z_{RX} = 50\Omega$.

From Table I, we find that M=6, n=3, $\tau_d = 80$ps, and $I_{max} = 7.41$mA should work. If $V_{swing} = 0.5$V and $\gamma = 1$, the minimum NF should be ~7dB according to equations 34 and 35. This example system was simulated in MATLAB to verify P_{ANT} and NF across the desired tuning bandwidth (Figure 20). Where $A_{TL} \approx 1$, the simulated NF closely matches the expected minimum NF, and the output power is +10dBm as desired. P_{ANT} drops and NF rises due to increasing transmission line loss as f_{TX} increases. The transmission line was modeled as described in Section III-C assuming $R_{sh} = 10\text{k}\Omega$, $L_{unit} = 1.333$nH, $Z_0 = 50\Omega$, and Q = 15.

APPENDIX
DERIVATION OF REJECTION ACROSS FREQUENCY

We start by using equation 3 to find the correct $\overrightarrow{w_{TX}}$ to cancel TX signal at f_{TX}. We choose $G_m = 1$ for simplicity and $V_{ANT} = 1$ and $V_{RX} = 0$ as usual:

$$\overrightarrow{w_{TX}} = \mathbf{Z_{TL}}^*[(\mathbf{Z_{TL}})\mathbf{Z_{TL}}^*]^{-1}\begin{bmatrix}1\\0\end{bmatrix} \tag{36}$$

To break this equation down, we start just by finding $(\mathbf{Z_{TL}}\mathbf{Z_{TL}}^*)$. Plugging in equation 9 for $\mathbf{Z_{TL}}$ gives:

$$\mathbf{Z_{TL}}\mathbf{Z_{TL}}^* = \begin{bmatrix}a & b\\ c & a\end{bmatrix}, \quad \text{where:}$$

$$a = \sum_{n=0}^{M-1}\alpha^{2n}\left(e^{-jn\phi}\right)\left(e^{jn\phi}\right) = \sum_{n=0}^{M-1}\alpha^{2n}$$
$$b = \sum_{n=0}^{M-1}\alpha^{M-1}\left(e^{-jn\phi}\right)\left(e^{j(M-1-n)\phi}\right)$$
$$c = \sum_{n=0}^{M-1}\alpha^{M-1}\left(e^{-j(M-1-n)\phi}\right)\left(e^{jn\phi}\right) \tag{37}$$

a, b and c can be simplified using the following sum identity,

$$\sum_{n=0}^{M-1}x^n = \frac{x^M-1}{x-1} \tag{38}$$

so that, omitting some algebra:

$$a = \frac{\alpha^{2M}-1}{\alpha^2-1} \quad \text{and} \quad b = c = \alpha^{M-1}\left(\frac{\sin(M\phi)}{\sin(\phi)}\right) \tag{39}$$

Plugging this result back into equation 36 gives:

$$\overrightarrow{w_{TX}} = \mathbf{Z_{TL}}^*\begin{bmatrix}\frac{\alpha^{2M}-1}{\alpha^2-1} & \alpha^{M-1}\left(\frac{\sin(M\phi)}{\sin(\phi)}\right)\\ \alpha^{M-1}\left(\frac{\sin(M\phi)}{\sin(\phi)}\right) & \frac{\alpha^{2M}-1}{\alpha^2-1}\end{bmatrix}^{-1}\begin{bmatrix}1\\0\end{bmatrix} \tag{40}$$

If we plug in $\mathbf{Z_{TL}}^*$ using equation 9 into equation 40, the n$^{\text{th}}$ element of $\overrightarrow{w_{TX}}$ is:

$$w_{TX,n} = \left(\alpha^{M-1}\right)S\left[\alpha^{-n}\left(\frac{\alpha^{2M}-1}{\alpha^2-1}\right)e^{j(M-1-n)\phi} - \alpha^n\left(\frac{\sin(M\phi)}{\sin(\phi)}\right)e^{jn\phi}\right]$$
$$S = \left[\left(\frac{\alpha^{2M}-1}{\alpha^2-1}\right)^2 - \alpha^{2M-2}\left(\frac{\sin^2(M\phi)}{\sin^2(\phi)}\right)\right]^{-1} \tag{41}$$

Now that we have found $\overrightarrow{w_{TX}}$ for our desired f_{TX}, we can calculate rejection for a frequency offset around f_{TX} using equation 2 (again assuming $g_m = 1$). If we define $\mathbf{Z_{TL}}[\omega]$ as the ideal transmission line impedance evaluated at ω, and $\overrightarrow{w_{TX}}(\omega)$ is given by equation 41 also at ω, then to find the rejection over some bandwidth Δf around a center frequency f_{TX}:

$$\begin{bmatrix}V_{ANT}\\ V_{RX}\end{bmatrix} = \mathbf{Z_{TL}}[2\pi(f_{TX}+\Delta f)]\cdot\overrightarrow{w_{TX}}(2\pi f_{TX}) \tag{42}$$

Substituting in our $\overrightarrow{w_{TX}}$ from equation 41 closed-form expressions for V_{ANT} and V_{RX} can be found. If we define rejection across frequency as $\text{Rej}(f) \equiv |\frac{V_{RX}}{V_{ANT}}|$, and plug in the closed-form expressions for V_{ANT} and V_{RX}, the result is given in equation 10.

ACKNOWLEDGMENT

The authors would like to thank Dong Yang for their insightful contributions. This material is based in part upon work supported by the DARPA Class program, Google, and NSF Grants 1247915 and 1641100. This paper is dedicated to the memory of Mark Rich, who was an early supporter of their ideas, and without whom this work may not have existed.

REFERENCES

[1] D.-J. van den Broek, E. A. M. Klumperink, and B. Nauta, "An in-band full-duplex radio receiver with a passive vector modulator downmixer for self-interference cancellation," *IEEE J. Solid-State Circuits*, vol. 50, no. 12, pp. 3003–3014, Dec. 2015.

[2] E. Kargaran, S. Tijani, G. Pini, D. Manstretta, and R. Castello, "Low power wideband receiver with RF self-interference cancellation for full-duplex and FDD wireless diversity," in *Proc. IEEE Radio Freq. Integr. Circuits Symp. (RFIC)*, Honolulu, HI, USA, Jun. 2017, pp. 348–351.

[3] M. Ingels *et al.*, "A 5 mm^2 40 nm LP CMOS transceiver for a software-defined radio platform," *IEEE J. Solid-State Circuits*, vol. 45, no. 12, pp. 2794–2806, Oct. 2010.

[4] V. Giannini *et al.*, "A 2-mm^2 0.1–5 GHz software-defined radio receiver in 45-nm digital CMOS," *IEEE J. Solid-State Circuits*, vol. 44, no. 12, pp. 3486–3498, Dec. 2009.

[5] R. Bagheri *et al.*, "An 800-MHz–6-GHz software-defined wireless receiver in 90-nm CMOS," *IEEE J. Solid-State Circuits*, vol. 41, no. 12, pp. 2860–2876, Nov. 2006.

[6] B. Analui, T. Mercer, S. Mandegaran, A. Goel, and H. Hashemi, "A 50 MHz–6 GHz, 2×2 MIMO, reconfigurable architecture, software-defined radio in 130 nm CMOS," in *Proc. IEEE Radio Freq. Integr. Circuits Symp.*, Tampa, FL, USA, Jun. 2014, pp. 329–332.

[7] Y. Cao and J. Zhou, "A CMOS 0.5-2.5 GHz full-duplex MIMO receiver with self-adaptive and power-scalable RF/analog wideband interference cancellation," in *Proc. IEEE Radio Freq. Integr. Circuits Symp. (RFIC)*, Boston, MA, USA, Jun. 2019, pp. 147–150.

[8] A. Ershadi and K. Entesari, "A 0.5-to-3.5 GHz self-interference-canceling receiver for in-band full-duplex wireless," in *Proc. IEEE Radio Freq. Integr. Circuits Symp. (RFIC)*, Boston, MA, USA, Jun. 2019, pp. 151–154.

[9] S. Subramanian and H. Hashemi, "A direct $\Delta\Sigma$ receiver with current-mode digitally-synthesized frequency—Translated RF filtering," in *Proc. IEEE Radio Freq. Integr. Circuits Symp. (RFIC)*, Philadelphia, PA, USA, Jun. 2018, pp. 92–95.

[10] S. Bu, S. Hameed, and S. Pamarti, "An LPTV noise cancellation technique for a 0.9-V filtering-by-aliasing receiver front-end with $>$67-dB stopband rejection," in *Proc. IEEE Custom Integr. Circuits Conf. (CICC)*, Austin, TX, USA, Apr. 2019, pp. 1–4.

[11] A. Nagulu and H. Krishnaswamy, "Non-magnetic CMOS switched-transmission-line circulators with high power handling and antenna balancing: Theory and implementation," *IEEE J. Solid-State Circuits*, vol. 54, no. 5, pp. 1288–1303, May 2019.

[12] G. Qi, B. van Liempd, P. Mak, R. P. Martins, and J. Craninckx, "A SAW-less tunable RF front end for FDD and IBFD combining an electrical-balance duplexer and a switched-LCN-path LNA," *IEEE J. Solid-State Circuits*, vol. 53, no. 5, pp. 1431–1442, May 2018.

[13] J. Zhou, T.-H. Chuang, T. Dinc, and H. Krishnaswamy, "Integrated wideband self-interference cancellation in the RF domain for FDD and full-duplex wireless," *IEEE J. Solid-State Circuits*, vol. 50, no. 12, pp. 3015–3031, Dec. 2015.

[14] S. Ramakrishnan, L. Calderin, A. Niknejad, and B. Nikolić, "An FD/FDD transceiver with RX band thermal, quantization, and phase noise rejection and $>$64 dB TX signal cancellation," *IEEE Radio Freq. Integr. Circuits Symp. (RFIC)*, Honolulu, HI, USA, Jun. 2017, pp. 352–355.

[15] T. Zhang, Y. Chen, C. Huang, and J. C. Rudell, "A low-noise reconfigurable full-duplex front-end with self-interference cancellation and harmonic-rejection power amplifier for low power radio applications," in *Proc. 43rd IEEE Eur. Solid State Circuits Conf. (ESSCIRC)*, Leuven, Belgium, Sep. 2017, pp. 336–339.

[16] H. Yüksel *et al.*, "A wideband fully integrated software-defined transceiver for FDD and TDD operation," *IEEE J. Solid-State Circuits*, vol. 52, no. 5, pp. 1274–1285, Jan. 2017.

[17] H. Yüksel, T. Tapen, Z. Boynton, E. Enroth, A. Apsel, and A. C. Molnar, "An FDD/FD capable, single antenna RF front end from 800 MHz to 1.2 GHz w/ baseband harmonic predistortion," in *Proc. IEEE Radio Freq. Integr. Circuits Symp. (RFIC)*, Philadelphia, PA, USA, Jun. 2018, pp. 120–123.

[18] B. Xiang, X. Wang, and A. B. Apsel, "A reconfigurable integrated dispersive delay line (RI-DDL) in 0.13-μm CMOS process," *IEEE Trans. Microw. Theory Techn.*, vol. 61, no. 7, pp. 2610–2619, Jul. 2013.

[19] H. Yüksel *et al.*, "Broadly tunable frequency division duplex transceiver: Theory and operation," in *Proc. IEEE Int. Conf. Electron., Circuits Syst. (ICECS)*, Monte Carlo, Monaco, Dec. 2016, pp. 688–691.

[20] T. Tapen, Z. Boynton, H. Yüksel, A. Apsel, and A. Molnar, "The impact of LO phase noise in N-path filters," *IEEE Trans. Circuits Syst. I, Reg. Papers*, vol. 65, no. 5, pp. 1481–1494, May 2018.

Thomas Tapen received the B.S. degree in electrical engineering and the M.S. degree from Cornell University, Ithaca, NY, USA, in 2015 and 2018, respectively.

His current research interests include RF, analog, and mixed-signal integrated circuit design focusing on integrated, software-defined duplexing transceivers.

Hazal Yüksel (S'14) received the B.S. degree in electrical engineering with a minor in mathematics from Duke University, Durham, NC, USA, in 2012, and the Ph.D. degree from Cornell University, Ithaca, NY, USA, in 2018. She currently holds an electrical engineering postdoctoral position with Columbia University, New York, NY.

Her current research interests include signal processing and adaptive radios.

Zachariah Boynton received the B.S. degree in electrical engineering from the University of Massachusetts Amherst, Amherst, MA, USA, in 2015, and the M.S. degree from Cornell University, Ithaca, NY, USA, in 2018.

His current research interests include RF, analog, and mixed-signal circuit design.

Alyssa Apsel (M'03–SM'10) received the B.S. degree from the Swarthmore College, Swarthmore, PA, USA, in 1995, and the Ph.D. degree from Johns Hopkins University, Baltimore, MD, USA, in 2002. She joined Cornell University, Ithaca, NY, USA, in 2002, where she is currently a Professor of electrical and computer engineering. She has authored or coauthored over 100 referenced publications in related fields of RF mixed-signal circuit design, ultralow-power radio, interconnect design and planning, photonic integration, and process invariant circuit design techniques, resulting in eight patents and several pending patent applications. Her current research interests include power-aware mixed-signal circuits and design for highly scaled CMOS and modern electronic systems. She received best paper awards at ASYNC in 2006 and the IEEE SiRF in 2012, the College Teaching Award in 2007, and the National Science Foundation CAREER Award in 2004. She was selected by Technology Review Magazine as one of the Top Young Innovators in 2004. She had a MICRO Top Picks Paper in 2006. She has served as an Associate Editor of various journals, including the IEEE TRANSACTIONS ON CIRCUITS AND SYSTEMS I and the IEEE TRANSACTIONS ON CIRCUITS AND SYSTEMS II, and has also served as the Chair of the Analog and Signal Processing Technical Committee of ISCAS 2011, as the Deputy Editor-in-Chief of the IEEE Circuits and Systems (CAS) Magazine, and on the Board of Governors of the IEEE CAS Society.

Alyosha Molnar received the B.S. degree from the Swarthmore College in 1997. He was an RFIC Design Engineer with Conexant Systems from 1998 to 2001, where he jointly developed their first generation direct-conversion receiver for the GSM cellular standard. Starting graduate school at the University of California at Berkeley in 2001, he was involved in early, ultralow-power radio transceivers for wireless sensor networks, and then he joined a retinal neurophysiology group, where he was also involved in dissecting the structure and function of neural circuits in the mammalian retina. He joined the Faculty at Cornell University in 2007, where he is currently an Associate Professor and focused on software-defined radios, neural interface circuits, integrated imaging techniques, and ultralow-power sensing.